Fatigue Damage Evolution in Silicon Films for Micromechanical Applications

by P. Shrotriya, S. Allameh, S. Brown, Z. Suo and W.O. Soboyejo

ABSTRACT—In this paper we examine the conditions for surface topography evolution and crack growth/fracture during the cyclic actuation of polysilicon microelectromechanical systems (MEMS) structures. The surface topography evolution that occurs during cyclic fatigue is shown to be stress-assisted and may be predicted by linear perturbation analyses. The conditions for crack growth (due to pre-existing or nucleated cracks) are also examined within the framework of linear elastic fracture mechanics. Within this framework, we consider pre-existing cracks in the topical SiO_2 layer that forms on the Si substrate in the absence of passivation. The thickening of the SiO_2 that is normally observed during cyclic actuation of Si MEMS structures is shown to increase the possibility of stable crack growth by stress corrosion cracking prior to the onset of unstable crack growth in the SiO_2 and Si layers. Finally, the implications of the results are discussed for the prediction of fatigue damage in silicon MEMS structures.

KEY WORDS—Fatigue, polysilicon, MEMS, surface topography evolution, crack growth

Introduction

Over the past few decades, single-crystal and polycrystalline silicon thin films have been used extensively in microelectromechanical systems (MEMS).[1,2] This has been due largely to their relatively high strengths (1–4.3 GPa)[3–5] and the prior knowledge of silicon microfabrication techniques that were inherited from the integrated circuits (IC) industry.[1] However, in many of the applications, such as accelerometers that deploy airbags in cars,[2] cyclic fatigue mechanism can occur at stresses well below the failure stresses under monotonic loading.[6–12] The cyclic fatigue mechanism may also be exacerbated by the effects of environment (especially water vapor), which accelerate the damage mechanisms under cyclic loading.[6]

The observed occurrence of cyclic fatigue in silicon MEMS structures was initially surprising due to the absence of prior reported fatigue damage for bulk silicon.[13,14] However, a number of research groups have confirmed that fatigue damage can occur in Si MEMS structures undergoing cyclic loading.[6–12] The studies have also shown that fatigue damage is accelerated in the presence of moisture,[6] notches, and compressive cycles.[15]

Two schools of thought have emerged with basic insights into the mechanisms of fatigue damage in silicon MEMS structures.[11,12,16,17] One school of thought has identified the importance of stress corrosion cracking phenomena (in the topical SiO_2 layer on Si) as the key process by which fatigue damage occurs in Si MEMS structures.[11,16] The other school of thought has suggested that surface topography evolution (again in the topical SiO_2 layer on Si) is an important process in the nucleation of fatigue damage in polysilicon.[12,17]

In an effort to clarify the relative importance of these two mechanisms, this paper examines the conditions for surface topography evolution and crack growth in Si MEMS structures. Following the introduction, brief descriptions of the material and experimental procedures are presented. The influence of stress on the evolution of surface roughness spectrum is investigated and surface topography evolution is then examined using linear perturbation analyses. Finally, the conditions for stable (stress corrosion cracking) and unstable crack growth in the topical SiO_2 layer are identified within a linear elastic fracture mechanics framework.

Material

The polysilicon MEMS structures that were used in this study were cantilevers with one end fixed, and the other connected to an interdigitating, capacitive driven comb drive; see Fig. 1(a). They were fabricated in batch runs at JDS Uniphase (formerly MCNC or Cronos Integrated Microsystems) of Raleigh-Durham, NC. Details of the fabrication process can be found elsewhere.[1] The gage section of the cantilevers had dimensions of $10 \times 10\ \mu m^2$, with a thickness of $2\ \mu m$. They were notched with the narrow section of the cantilever being $5\ \mu m$ directly beneath the notch. Figure 1(b) shows a scanning electron microscopy (SEM) image of a notched sample. The image reveals a nanoscale structure with an average grain size of about 200 nm; see Fig. 1(b). The microstructure of the polysilicon resonant structure is pore-free except for deeper cusps at some triple joints. These deeper cusps have the appearance of porosity; however, polysilicon cross-sections observed in our focused ion beam (FIB), and TEM work have shown solid pore-free structure.

Experimental Procedure

A topical SiO_2 layer seals the polysilicon MEMS structures in the as-received condition. The MEMS structures were

P. Shrotriya is a Post-Doctoral Researcher, S. Allameh is a Staff Scientist, Z. Suo is a Professor and W.O. Soboyejo (soboyejo@princeton.edu) is a Professor, Princeton Materials Institute and Department of Mechanical and Aerospace Engineering, Princeton University, Princeton, New Jersey 08544. S. Brown is an Office Director and Principal Engineer, Exponent Failure Associates, Natick, MA 01760.

Original manuscript submitted: February 7, 2003.
Final manuscript received: February 7, 2003.

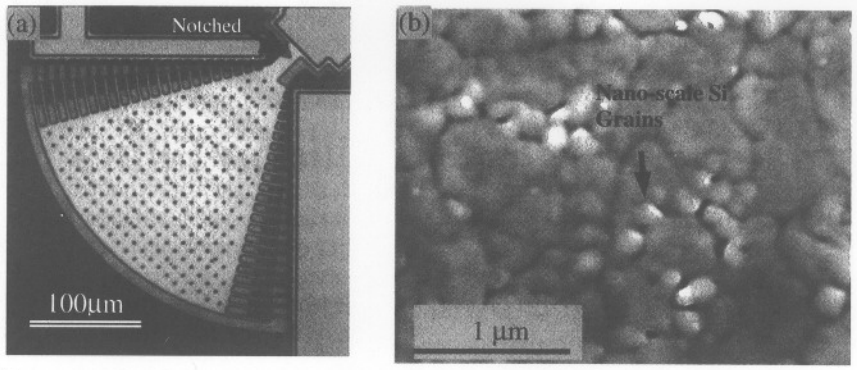

Fig. 1—Notched polysilicon sample: (a) photograph of a notched comb drive structure; (b) SEM micrograph of the polysilicon MEMS structure before actuation

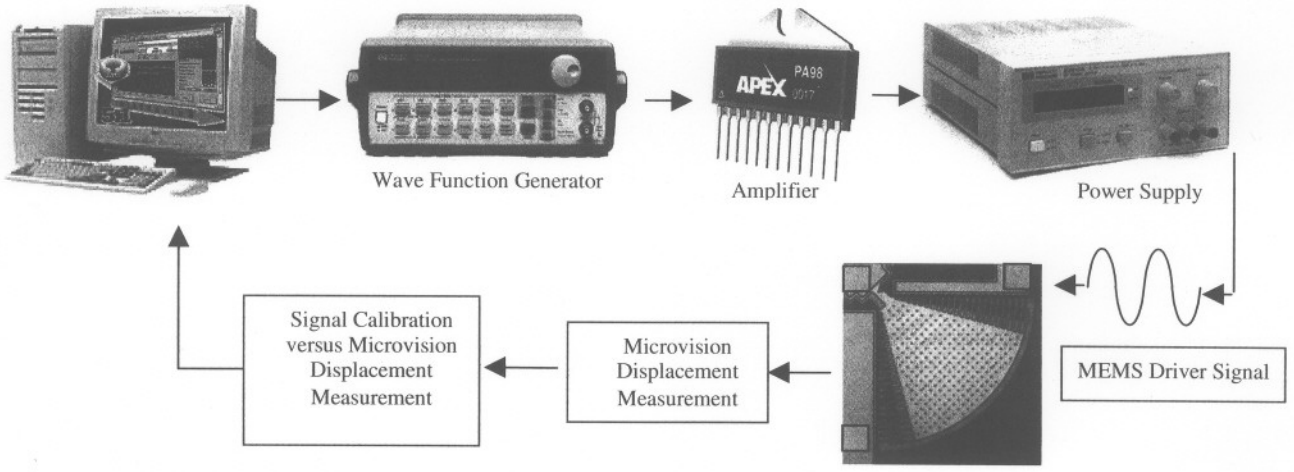

Fig. 2—Experimental setup for actuation of the MEMS cantilever structure

released by a 5 min soak in 49.6% hydrofluoric acid (HF), followed by a 10 min soak in water and a 10 min soak in methanol. The samples were dried in air by placing them on a hot plate with a surface temperature of 110°C for 2 min. Gold wire bonding was performed to connect the contact pads of the devices to an edge connector.

Details of the actuation of the sample are shown schematically in Fig. 2. The actuation of the samples was performed in ambient air (75% relative humidity) at room temperature (~25°C), using an alternating current (ac) signal from a Hewlett-Packard wavefunction generator and amplified by an APEX amplifier to levels between 0–250 V. The frequency of the drive was chosen such that it would synchronize with the first harmonic of the devices (~40.9 kHz for the notched samples). This was verified experimentally by imaging the device oscillating in one direction with a strobe light frequency of 40.2 kHz. Upon doubling of the strobe frequency, the resulting double images revealed the bi-directional motion of the device, as expected at such a frequency.

To measure the angular displacement of the cantilever, micrographs obtained from an optical microscope were analyzed. The details of microvision techniques that were used for the displacement measurements are shown in Fig. 3. An ultra-bright green light emitting diode (LED) was powered at a frequency slightly less than that of the device. This allowed the device to be observed with a slow motion that was recorded and analyzed frame-by-frame using an image analysis software package obtained from National Instruments, Austin, TX. The magnitude of angular displacement was obtained from the amplitude of a sine wave curve, and fitted to the displacement versus time graph. The angular displacement was found to be linearly proportional to the square of actuation voltage. The resulting calibration curve obtained for a range of actuation voltages between 35 and 145 V is presented in Fig. 3(b) and the best-fitting approximation is

$$\phi = \frac{8V^2}{100000} \tag{1}$$

where ϕ is the angular displacement in degrees and V is the actuation voltage in volts.

In situ atomic force microscopy (AFM) was used to study the evolution of surface topography at the bottom of the notch, where the stresses are relatively high. Tapping-mode AFM allowed non-contact imaging of the surface during actuation. Two different studies were utilized to study the influence of the stress on the surface topography evolution. In the first

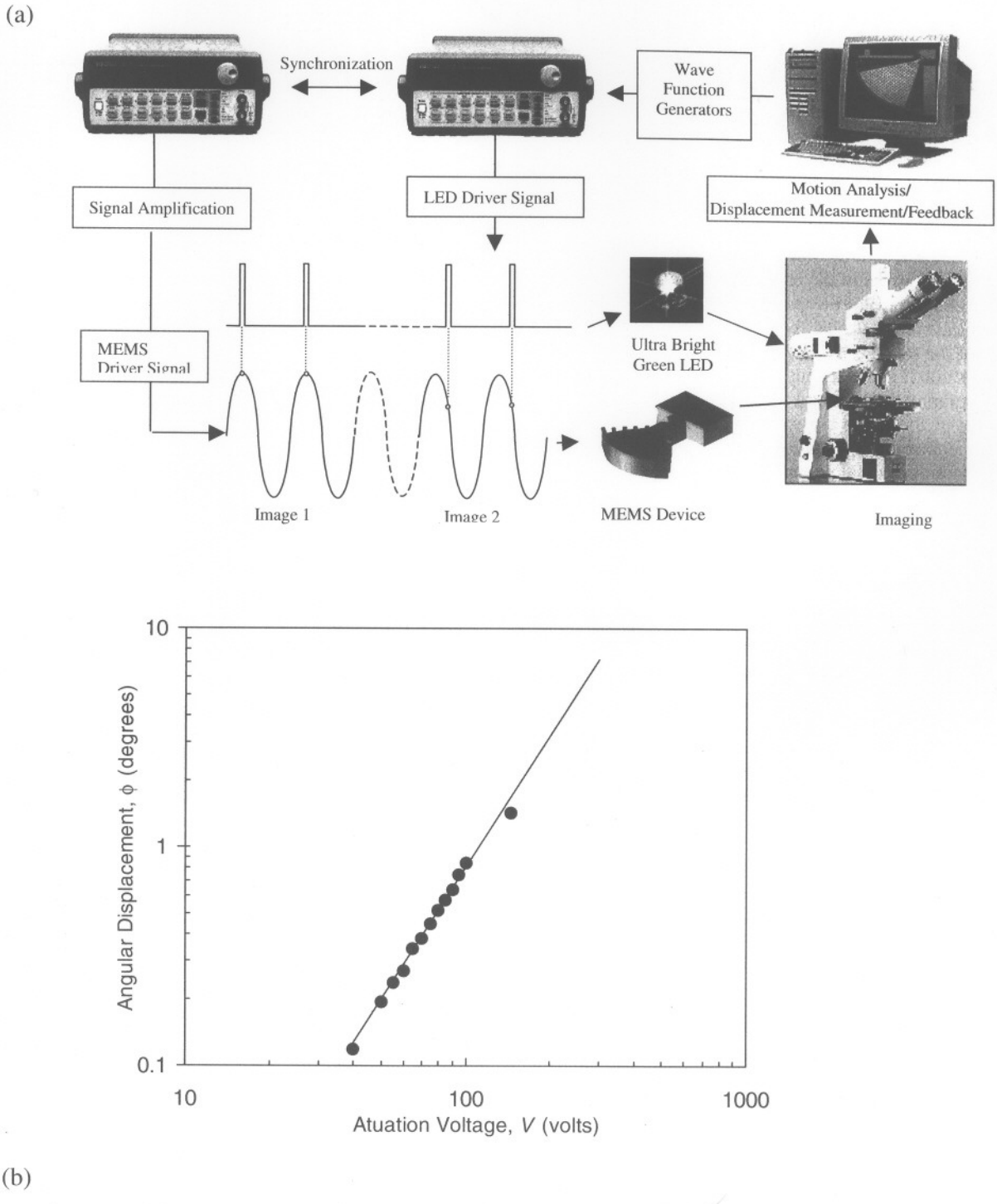

Fig. 3—Calibration of the MEMS structure: (a) experimental setup; (b) calibration curve

study, the structures were oscillated for fixed times at progressively increasing actuation voltages from 125 to 210V. In the second study, the actuation voltage was held constant at 125 V and the structures were oscillated until failure. Continuous recording of images allowed quantitative measurement of the extent of change in surface topography as a function of the number of fatigue cycles and actuation voltage.

Finite Element Analysis

As a first step in the analysis of the surface topography evolution, finite element analysis was utilized to determine the relationship between the observed angular displacement and stress distribution around the notch tip. Finite element analysis was performed, not only for the sample, but also for the whole suspended mass, including the drive structure.

The model was constructed from the 6,200 six-node plane stress triangular elements. The mesh density was determined by a study of the numerical convergence of stress distribution with the number of elements. For the analysis, Young's modulus and Poisson's ratio of polysilicon were assumed to be 169 GPa and 0.22, respectively,[18] and a linear elastic small strain formulation was used. The finite element analysis was performed using ABAQUS.

The results of the finite element analysis are presented in Fig. 4. Figures 4(a) and (b) respectively present the details of the discretization near the notch tip and the contour of maximum principal stress in the region surrounding the notch tip corresponding to an angular displacement of 1.44°. The highest magnitude of stress was associated with an area in the near vicinity of the notch root. The concentration of high stresses at the root notch is consistent with the highest extent of surface topography evolution in this area. The maximum stress developed at the notch tip varies linearly with the angular displacement of the structure. The linear calibration relating the maximum principal stress and the angular displacement is found to be

$$\sigma_{max} = 1.9 \times 10^9 \, \phi, \tag{2}$$

where σ_{max} is in Pa and angular displacement, ϕ, is in degrees.

Surface Topography Evolution

Typical scanned images obtained from *in situ* AFM are presented in Fig. 5. The surface of the unactuated sample is imaged on a 2×2 μm^2 scale in Fig. 5(a). A corresponding image obtained after actuation is presented in Fig. 5(b). Similar images covering larger areas under the notch are presented on a 5×5 μm^2 scale in Figs. 5(c) and 5(d) for the unactuated and actuated surfaces, respectively. The change in the surface topography is quite evident from these images. The arrows show the location of the bottom of the notch on the three-dimensional (3D) images.

The increase in actuation voltage leads to larger angular displacement of the cantilever structure, which in turn results in higher stresses at the notch tip. The influence of the actuation voltage on the evolution of surface topography was quantified by comparing the surface roughness spectrum of fast Fourier transform (FFT) of the corresponding *in situ* AFM images to the AFM image before actuation. Following the procedure described by Kim et al.,[19] the quantity $\ln\left[q(\omega, t)/q(\omega, 0)\right]$ was evaluated using the measured surface morphologies of the MEMS structure corresponding to the different actuation voltages. Figure 6 plots the contours of $\ln\left[q(\omega, t)/q(\omega, 0)\right]$ corresponding to the areas of 1×1 μm^2 at the different voltages, near the notch tip. In the contour plot, the Fourier components of surface roughness whose amplitudes increase with time are indicated by the positive contours, and the components whose amplitudes are decreasing are indicated by negative contours. Comparison of the contour plots indicates that the shape of the contours is similar, indicating that amplitudes of only a few frequencies among surface roughness spectrum grow with time. Additionally, the maximum value of $\ln\left[q(\omega, t)/q(\omega, 0)\right]$ increases progressively, increasing actuation voltage of the cantilever structure. The calibration curve (see Fig. 3(b)) was used to compute the angular displacement of the cantilevers corresponding to the different actuation voltages. The maximum values of $\ln\left[q(\omega, t)/q(\omega, 0)\right]$ at different actuation voltages are plotted against the actuation voltage of the structure in Fig. 7. The stress distribution around the notch tip is directly proportional to the angular displacement of the cantilever. Consequently, the monotonic increase of $\ln\left[q(\omega, t)/q(\omega, 0)\right]_{max}$ with increasing angular displacements clearly indicates that the evolution of surface topology is accelerated with an increase in stress around the notch tip.

The comparison of the surface roughness spectra quantifies the overall evolution of the surface topography with increasing actuation voltage. A close observation of the surface morphologies indicates that the evolution of the surface roughness spectrum is associated with deepening and sharpening of pre-existing grooves on the silicon surface. In order to elucidate this mechanism, the evolution of five different grooves of almost equal initial depth was studied. The location of the grooves with respect to the notch tip is schematically indicated in Fig. 8(a). The *in situ* AFM images were registered using an image registration MATLAB (Mathworks Inc., Natick, MA) code based on algorithms described by Bergen et al.[20] The registered images were analyzed to determine the change in depth of the grooves with time and increasing actuation voltages. The measured groove depths are normalized with the initial depth in order to facilitate comparison of growth rates between the different grooves. The normalized groove depths are plotted as a function of time in Fig. 8(b). As shown in Fig. 8(b), the depth of all five grooves increases with time and the depth evolution is accelerated with the increase in actuation voltage. The groove closest to the notch tip deepens at a faster rate compared to the other grooves. The depth evolution decreases monotonically as the distance from the notch tip increases. The above observations clearly indicate that the groove depth evolution is dependent on the stress field. The grooves closer to the notch tip are subjected to higher stresses and, consequently, deepen at a faster rate. In addition, the increase in actuation voltage increases the magnitude of overall stress field and, as a result, depth evolution of all the grooves is accelerated.

In the second set of experiments, the actuation voltage was kept constant at 125 V and the cantilever structures were actuated until failure. The *in situ* AFM images were registered with respect to the AFM image of the cantilever before actuation. The surface roughness spectrum obtained from the registered *in situ* AFM images was compared with the initial spectrum in order to elucidate the evolution of surface morphology with time. Following the procedure described by Kim et al.,[19] the quantity $\ln\left[q(\omega, t)/q(\omega, 0)\right]$ was evaluated using the measured surface morphologies of the MEMS structure at different times. The contours of $\ln\left[q(\omega, t)/q(\omega, 0)\right]$ corresponding to the 1×1 μm^2 area near the notch tip for AFM images captured at different times are plotted in Fig. 9. Comparison of the contour plots indicates that the shape of the contours is similar indicating that amplitudes of only a few frequencies among the surface roughness spectrum grow with time. In addition, the comparison of contour plots corresponding to different times indicates that the maximum value of $\ln\left[q(\omega, t)/q(\omega, 0)\right]$ increases with time. The maximum values of $\ln\left[q(\omega, t)/q(\omega, 0)\right]$ are plotted as a function of the actuation time in Fig. 10. The maximum value of $\ln\left[q(\omega, t)/q(\omega, 0)\right]$ increases monotonically with time within the experimental scatter, indicating that the surface topography evolution observed during actuation is a gradual and monotonic process.

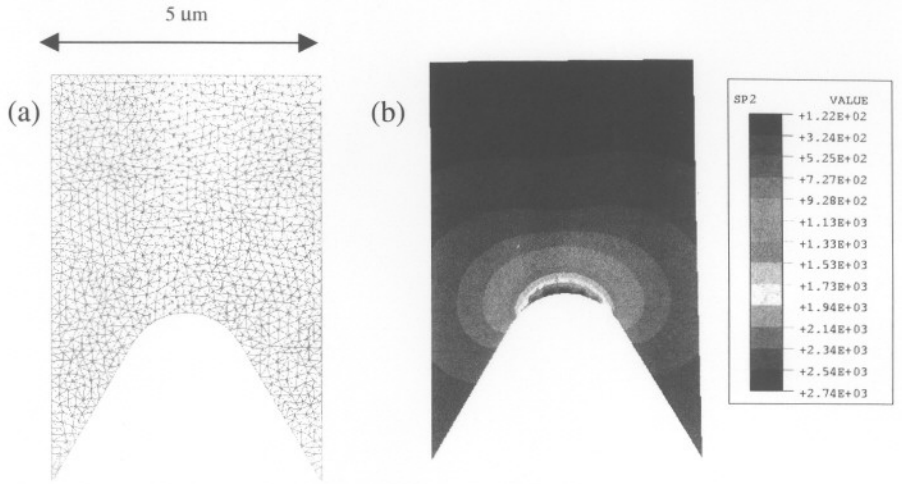

Fig. 4—Finite element calculations: (a) details of the discretization near the notch tip; (b) maximum principal stress distribution near the notch tip corresponding to an angular displacement of 1.44°

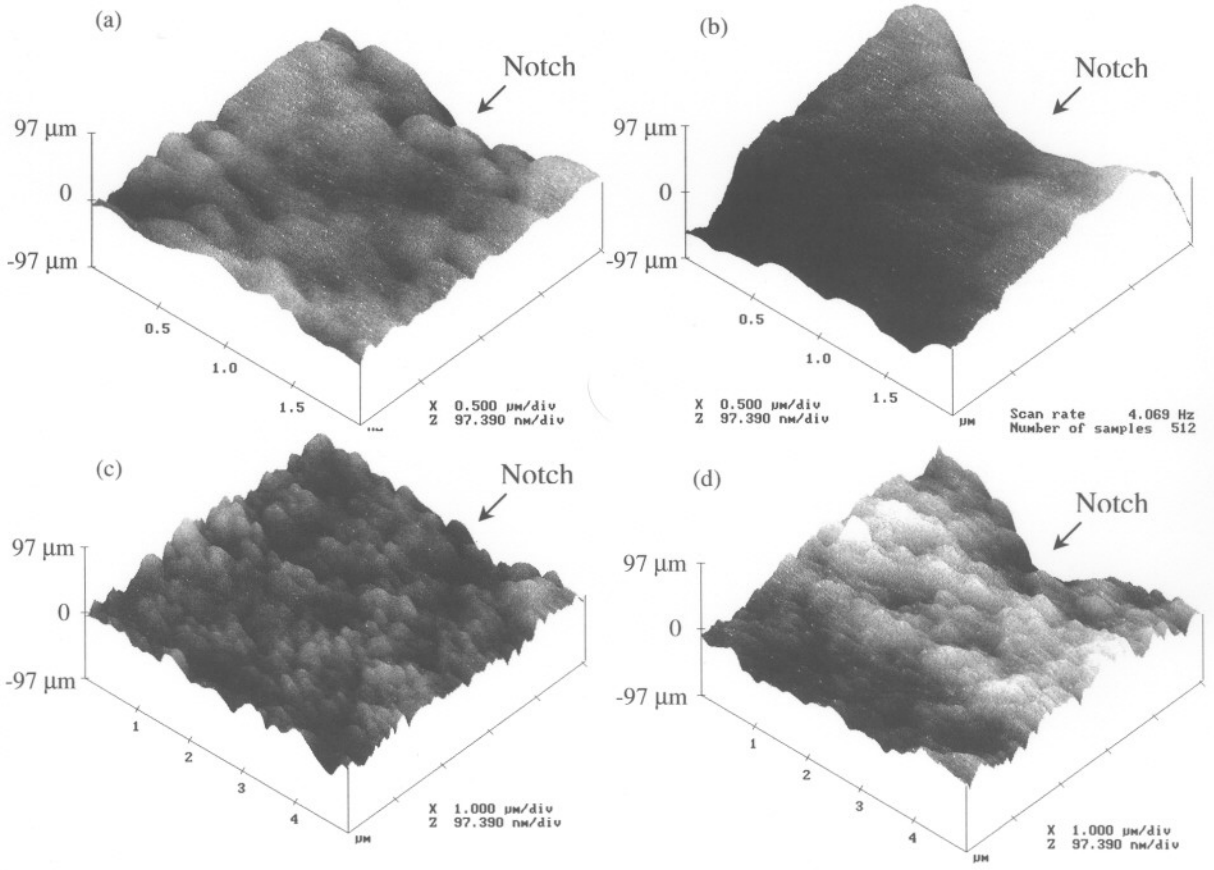

Fig. 5—AFM images showing surface evolution of the silicon MEMS sample under cyclic loading conditions: (a), (c) before actuation (2 and 5 μm scale respectively); (b), (d) after actuation (2 and 5 μm scale respectively)

The *in situ* AFM images acquired during the actuation of the cantilever at a constant voltage were also analyzed to investigate the evolution of individual grooves. A careful observation of the AFM images revealed that only the grooves located in front of the notch tip show a discernable change in depth with time. Five different grooves of similar initial depth located around the notch tip were identified. The locations of the different grooves are indicated on the AFM image in Fig. 11(a). As shown in Fig. 11(a), the identified grooves are distributed in front and before the notch tip. The registered AFM images were analyzed to determine the evolution of the depth of each groove with time. The measured

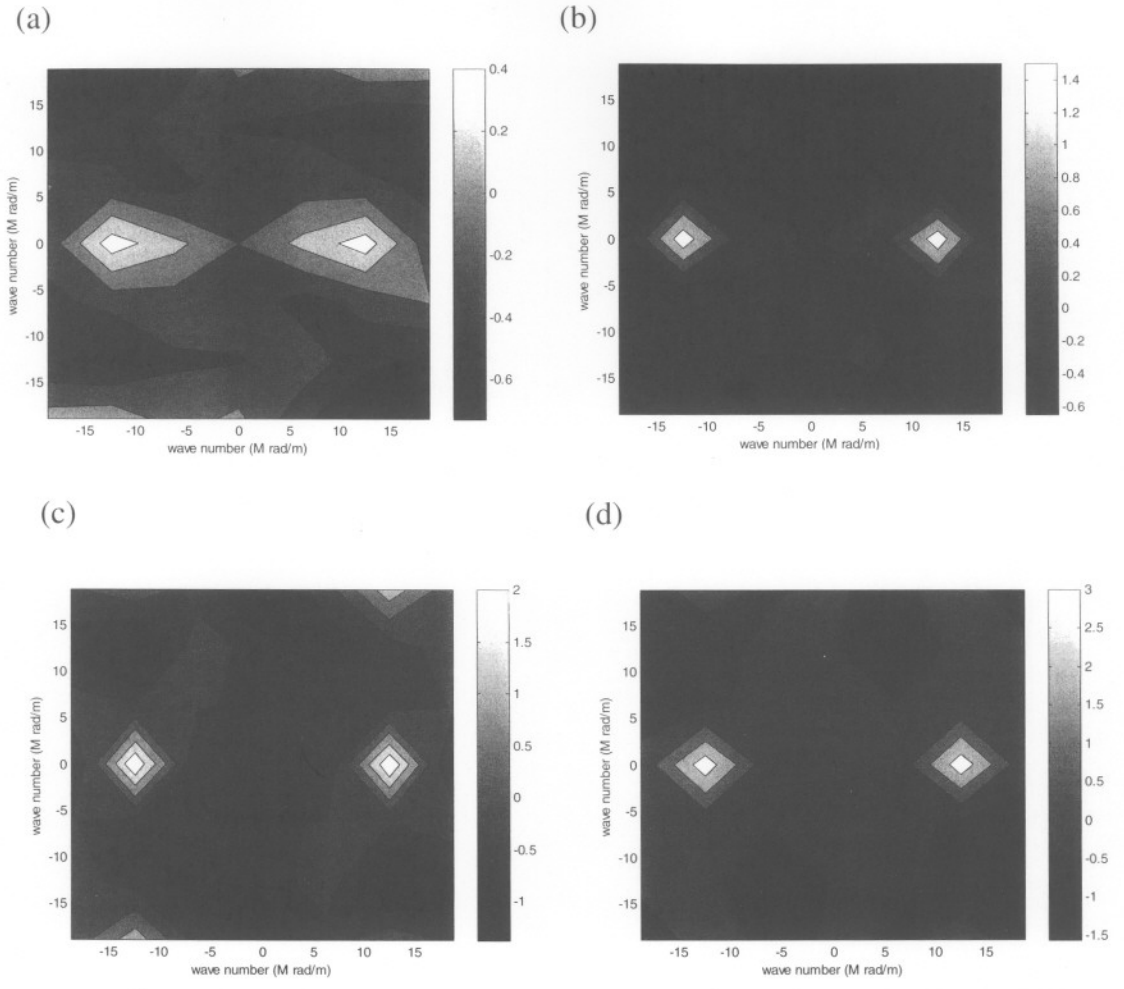

Fig. 6—Contours of $\ln\left[q(\omega, t)/q(\omega, 0)\right]$ corresponding to an area of $1 \times 1\ \mu m^2$ near the notch tip at different actuation voltages: (a) 160 V; (b) 185 V; (c) 200 V; (d) 215 V

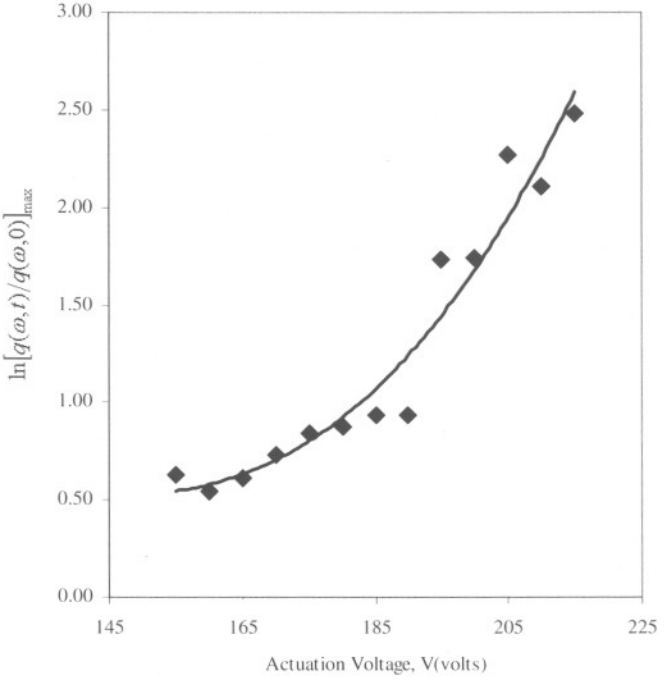

Fig. 7—Plot of $\ln\left[q(\omega, t)/q(\omega, 0)\right]_{max}$ at different actuation voltages

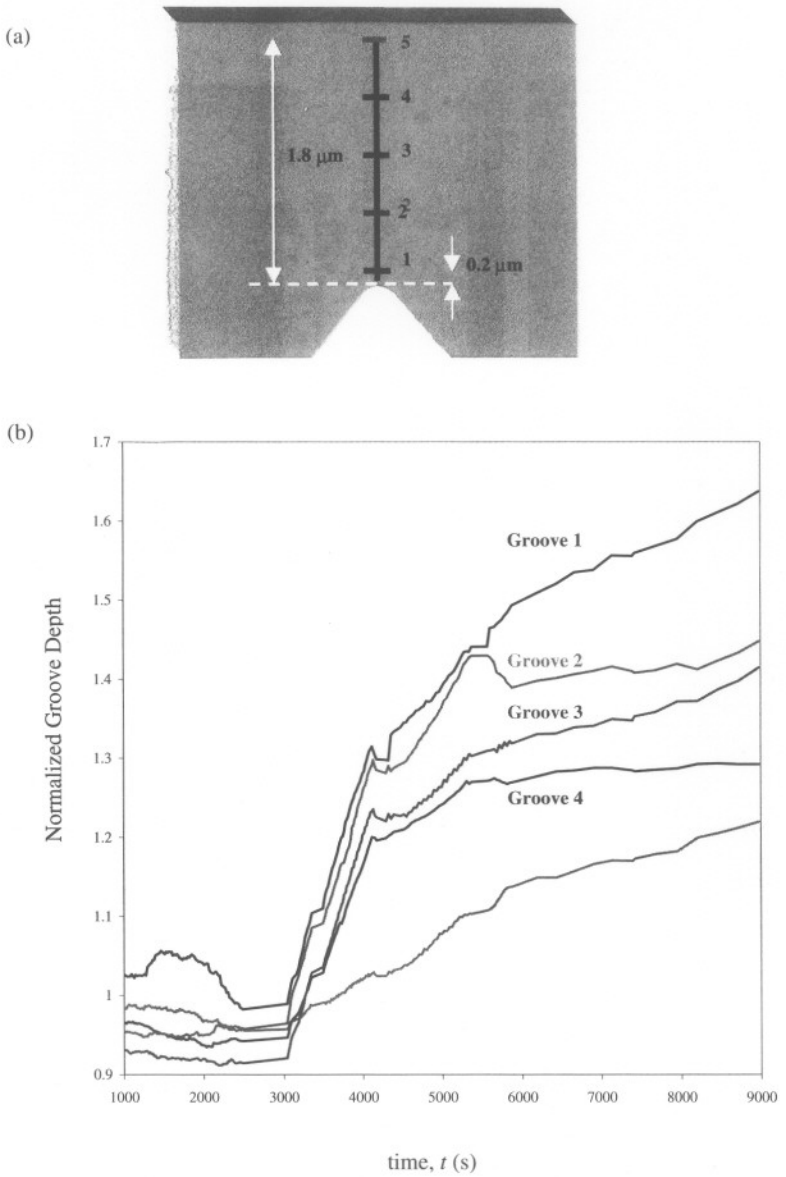

Fig. 8—Deepening of groove during actuation at different voltages: (a) groove locations; (b) normalized groove depth plotted as a function of time

groove depths are normalized with the initial depth in order to facilitate comparison among the five different locations. The normalized depths of the five different grooves are plotted in Fig. 11(b). The grooves (1 and 2 in Fig. 11(a)), located behind the notch tip, show no discernable change in depth with time whereas the grooves (3, 4 and 5 in Fig. 11(a)), located in front of the notch tip, progressively deepen with time. The groove located right at the base of the notch tip shows the most rapid evolution of depth with time. The rate of depth evolution decays as the distance of the groove from the notch tip increases. The groove depth evolution observations are in exact correlation with the stress field around the notch tip. The values of principal stresses are highest at the base of the notch tip and their values gradually decay with increasing distance in front of the notch tip. The locations corresponding to grooves 1 and 2 develop no stress concentration during actuation. The correlation between the stress field and observations on the groove depth evolution clearly reaffirms the hypothesis that the surface roughness evolution is a stress-assisted process. This particular cantilever structure was actuated until final failure at a constant actuation voltage of 125 V. The AFM image of the fractured cantilever is shown in Fig. 11(c). A comparison of the *in situ* AFM images acquired during the actuation and the AFM images of the fractured sample reveals that fracture plane coincides with groove 3 located at the base of the notch tip.

Linear Perturbation Analysis

The observed changes in the surface topography may be ascribed to a stress assisted dissolution of SiO_2 that can give rise to the evolution of grooves and ultimately to the

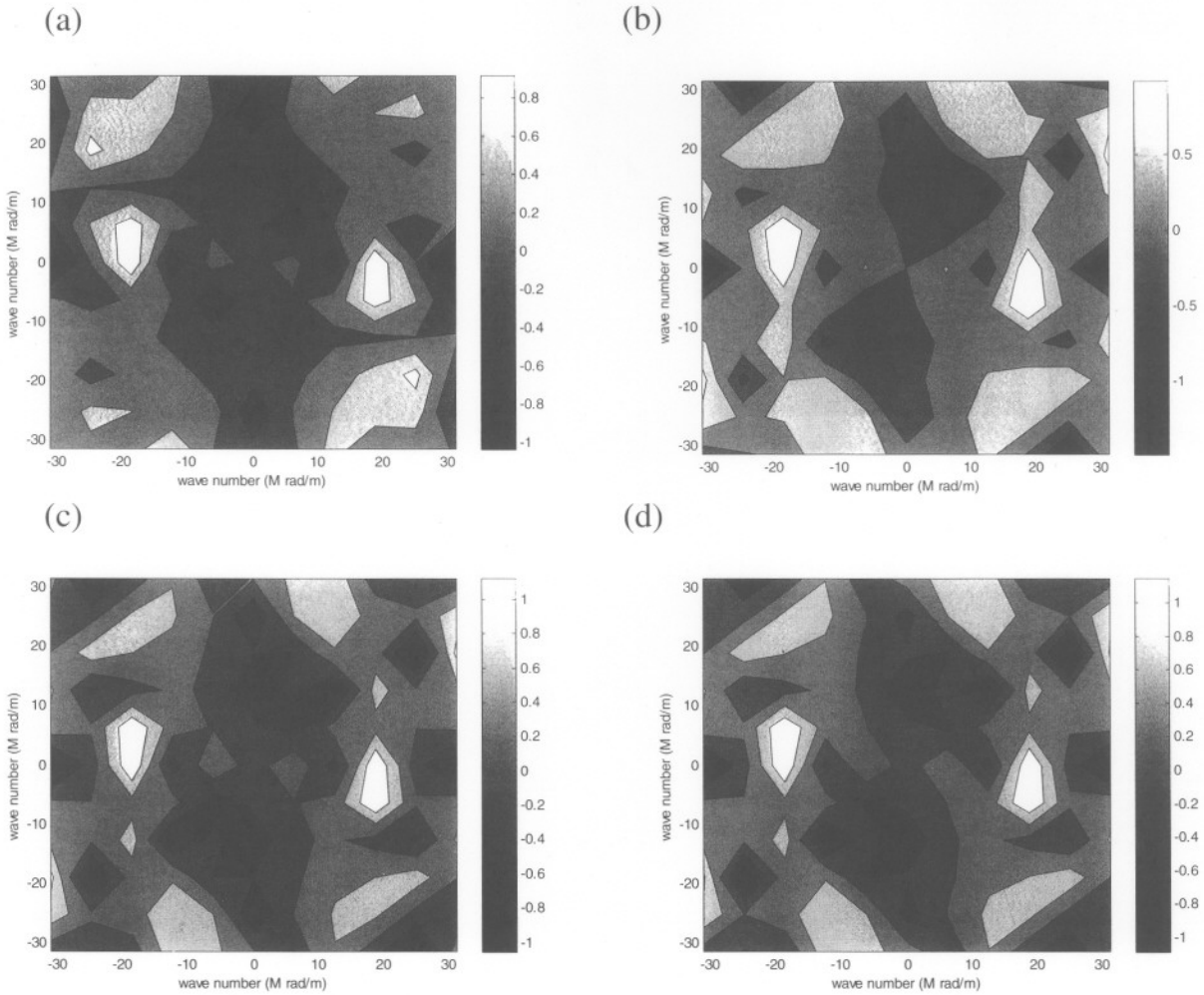

Fig. 9—Contours of $\ln\left[q(\omega,t)/q(\omega,0)\right]$ corresponding to an area of 1 × 1 μm^2 near the notch tip at different times during actuation at 145 V: (a) t = 4,000 s; (b) t = 8,000 s; (c) t = 12,000 s; (d) t = 16,000 s

nucleation of fatigue cracks.[21,22] The dissolution reaction is influenced by both surface energy and strain energy of the stressed surface. Mullins[23] studied the effect of surface energy on the evaporation of a solid. If a solid is perturbed into a wavy shape, the surface energy causes the solid to evaporate faster at the crests than at troughs, so that the wave amplitude decays over time, and the surface flattens. Srolovitz[24] studied the effect of stress. For a wavy surface, a stress applied to the surface induces a non-uniform stress field; the magnitude of the stress is larger at troughs than at crests. Consequently, the solid evaporates faster at the troughs than at crests, so that the wave amplitude grows over time and the surface roughens.

When both the surface energy and stress act together, the ratio of the surface energy to the elastic energy defines a length scale; shorter wavelengths decay and longer wavelengths grow. Kim et al.[19] and Yu and Suo[25] used linear perturbation analysis to study the dissolution of a stressed solid surface and related the change in surface profile to the stress state. A similar analysis is utilized here to study the observed roughening of the SiO_2 layer on the MEMS structure. For the sake of brevity, the analysis is summarized briefly and the reader is referred to Yu and Suo[25] for details.

Following Yu and Suo[25] the driving force of the dissolution reaction for a solid under a state of stress and with a curved surface is expressed as

$$F = g - w - K\gamma. \tag{3}$$

Here, g is the free energy difference between the atoms in two bulk phases (i.e., the environment and the unstressed solid), w is the elastic energy per unit volume, γ is the surface energy per unit area and K is the sum of principal curvatures. The reaction rate, R, is assumed to vary linearly with the driving force, namely

$$R = MF. \tag{4}$$

The proportionality constant, M, is known as the mobility of the surface and in the present analysis is assumed to be independent of stress.

The SiO_2 layer is subjected to the in-plane stress state. The principal stresses and principal axes are denoted by σ_1 and σ_2, and x_1 and x_2, respectively. The height, $H(x_1, x_2, t)$, of the surface is decomposed into the average height, $H_0(t)$, and the surface roughness, $h(x_1, x_2, t)$:

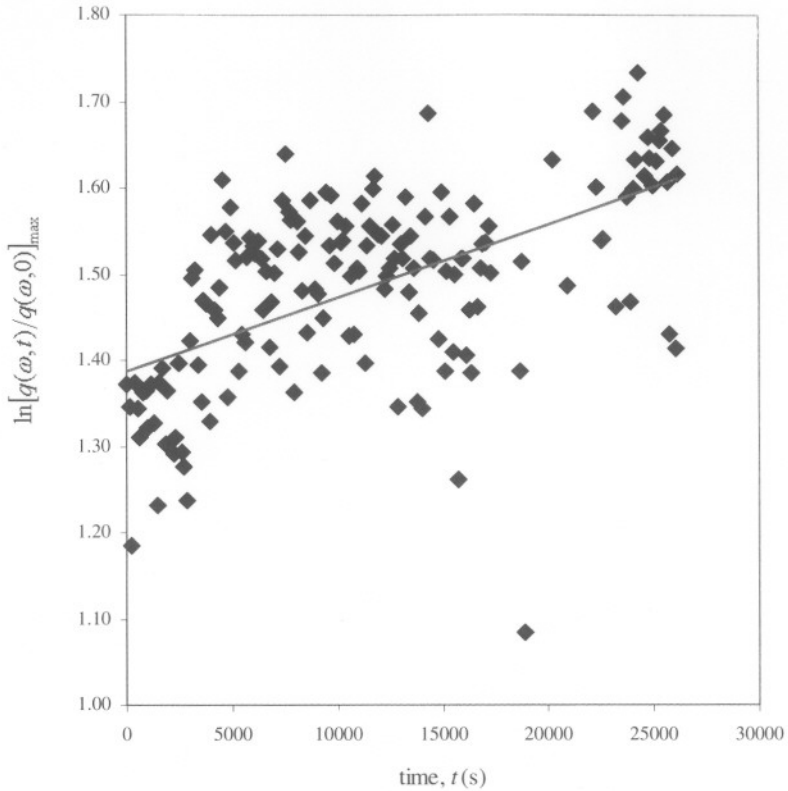

Fig. 10—Plot of $\ln\left[q(\omega, t)/q(\omega, 0)\right]_{max}$ as a function of time during actuation at 125 V

$$H(x_1, x_2, t) = H_0(t) + h(x_1, x_2, t). \tag{5}$$

The roughness of the surface is a linear superposition of the Fourier components of wave vectors (lying in the x_1–x_2 plane) of all magnitudes and directions. When the wave amplitude is small, to the first order in wave amplitude, the time evolution of one Fourier component is independent of another. Consequently, only one Fourier component need be analyzed. A wave vector of magnitude ω pointing in the direction x which is at an angle θ from the x_1-axis is illustrated in Fig. 12 and is represented as

$$h = q(\omega, t)\cos \omega x. \tag{6}$$

The wave amplitude is assumed to be small compared to the wavelength namely, $\omega q \ll 1$, for the linear perturbation analysis. The Fourier component is considered a small perturbation and results are retained up to the leading term in the wave amplitude q. To the leading order in q, the reaction rate is[25]

$$R = \frac{dH_0}{dt} + \frac{\partial h}{\partial t}. \tag{7}$$

Similarly, the driving force, F, to the leading order in q is obtained as[25]

$$F = F_0 + \alpha h \tag{8}$$

where F_0 is the driving force for a perfectly flat surface subjected to σ_1 and σ_2 principal stresses, α is expressed in terms of stress state and material properties as

$$\alpha = \frac{2(1+\nu)}{E}\left[(1-\nu)\left(\sigma_1 \cos^2\theta + \sigma_2 \sin^2\theta\right)^2 + (\sigma_1 - \sigma_2)^2 \cos^2\theta \sin^2\theta\right]\omega - \gamma\omega^2, \tag{9}$$

and E and ν are the Young's modulus and Poisson's ratio of the material, respectively. From eqs (4), (7) and (8), it can be concluded that

$$\frac{\partial h}{\partial t} = M\alpha h. \tag{10}$$

The expression in eq (10) is integrated with respect to time in order to obtain[25]

$$\ln \frac{q(\omega, t)}{q(\omega, 0)} = M\alpha t. \tag{11}$$

Hence, when the quantity α is positive, the amplitude of the corresponding wavelength grows with time, and when it is negative the amplitude of wavelength decays with time.

The quantity, α, corresponding to the stress state at base of the notch, is evaluated for the different Fourier components in order to study the influence of the stress-assisted surface reaction. During the experiment, the MEMS structure is loaded under cyclic loading in the experiment, thus the stress field at the notch tip is alternately tensile and compressive during one cycle. In the present formulation, the quantity, α, is dependent only on the square of the stress at the notch tip and,

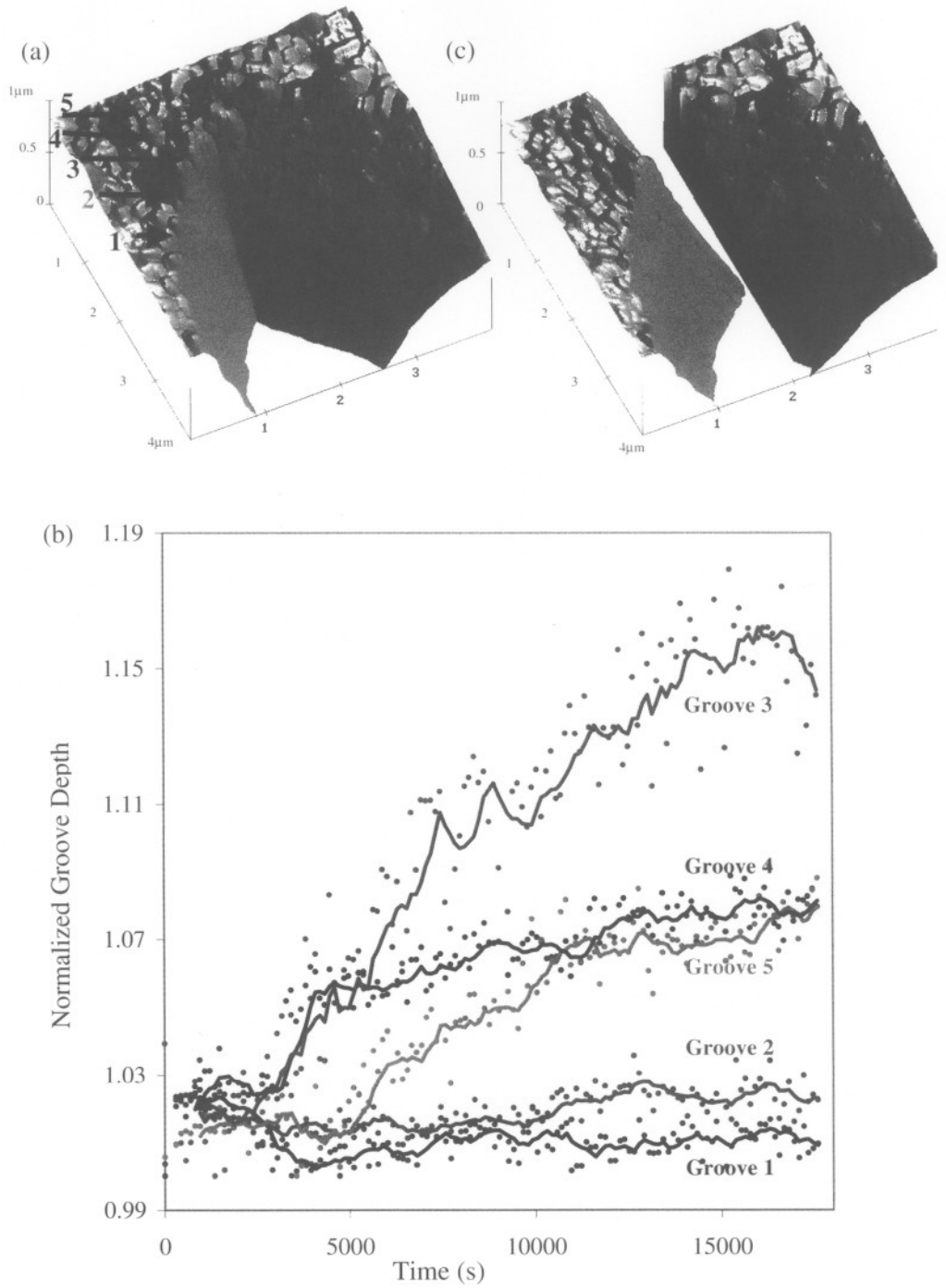

Fig. 11—Deepening of groove during actuation at a constant voltage of 125 V: (a) groove locations; (b) normalized groove depth plotted as a function of time (c) Final fracture surface path passes through groove 3

hence, its value is only influenced by the magnitude of the stress field. Consequently, the root-mean-square (rms) average of principal stresses is utilized in the calculations in order to account for the cyclic loading. The finite element model described in previous section is utilized to compute the rms average of the in-plane stresses at the base of the notch. The rms averages of stresses are $\sigma_{11} = 1990$ MPa, $\sigma_{22} = 141$ MPa, and $\sigma_{12} = 0$. The interfacial energy of the SiO_2 and water system is reported equal to 4.8 Jm^{-2}.[26] The stress state and interfacial energy values are substituted in eq (9) in order to express α as a function of Fourier components of the surface roughness. The contour plot of α corresponding to the present stress state is presented in Fig. 13. The dark thick contour line on the plots corresponds to $\alpha = 0$ and α is positive for all the wavenumbers enclosed by it.

The quantity on the left-hand side of eq (10) represents the evolution of Fourier components of surface roughness with time. Comparison of the contour plots of

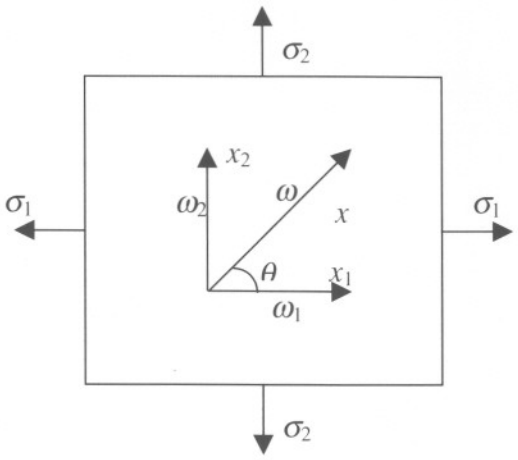

Fig. 12—Geometrical conventions used in the model

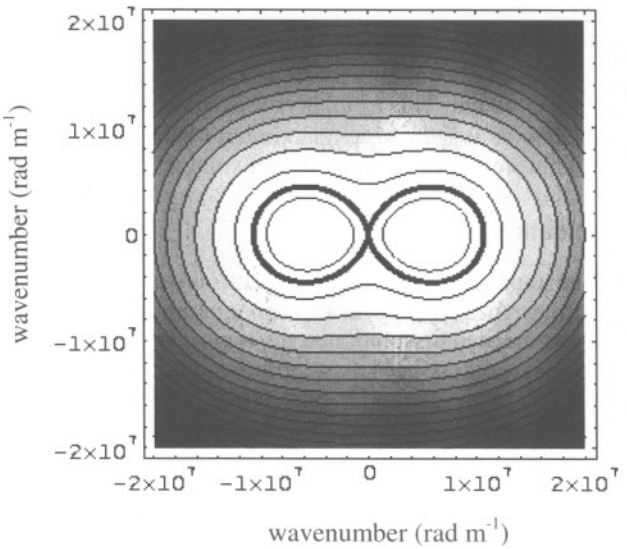

Fig. 13—Contours of α corresponding to the stress state at the notch tip during actuation at 125 V

$\ln\left(q(\omega, t)/q(\omega, 0)\right)$ and α indicates that the shape of the contours is similar. Additionally, the magnitude of wavenumbers predicted to grow by linear perturbation analysis compares remarkably well the experimental measurements.

It is particularly interesting to note that the wavelengths for which topography evolution occurs (~300 nm) is comparable to the average grain size of the polysilicon (~200 nm). This suggests that the topical (amorphous) SiO_2 structure retains some "memory" of the underlying microstructure. Visual evidence of such "memory" is apparent in the SEM and AFM images of the polysilicon structures (Figs. 1(b) and 5). The images reveal an underlying polysilicon grain structure that is templated into the groove structure. Further work is clearly needed to examine the potential effects of such grain structures on surface topography evolution and crack nucleation mechanisms in polysilicon MEMS structures. Such work is beyond the scope of the current paper.

In summary, the above results show clearly that surface topography evolves in polysilicon MEMS structures during cyclic actuation. The surface topography evolution occurs in the high stress regions in the vicinity of notches. However, the stresses are not sufficient to cause surface topography evolution away from the notches. It is also important to note that the wavelengths that grow are consistent with predictions from a linear perturbation model in which surface topography evolution is assumed to occur due to the stress-assisted dissolution of silica. Finally, it is interesting to note that the critical wavelength is comparable to the average grain size of the polysilicon substrate.

As discussed in the materials section, there are some triple joint cusps that appear as porosity in the SEM image of Fig. 1(b). While these could potentially act as crack nucleation sites, none of these cusps may lead to the nucleation of cracks under cyclic loads used in this experiment. This is supported by the results of Brown et al.[6] and Muhlstein et al.[11] who isolated the effects of stress-assisted dissolution of topical SiO_2 by careful environmentally controlled experiments. They concluded that, in the absence of water vapor, the resonant structures could have infinite life under cyclic loading conditions similar to ours. This signifies that the presence of cusps is not sufficient for crack nucleation. Rather, evolution of surface perturbations (including pre-existing boundary cusps) into sharper and crack-like grooves is presumably precursor to crack nucleation. Further evaluation of surface topography evolution at lower humidity levels is necessary to strengthen the validity of this hypothesis.

Crack Growth Scenarios

The above discussion has focused essentially on the evidence for stress-assisted surface topography evolution. As discussed earlier, there is considerable evidence for stress corrosion cracking in the topical SiO_2 layer, obtained by Muhlstein et al.[16] using high voltage (about two million) transmission electron microscopy (TEM) imaging of the notch-tip regions in a similar MEMS structure actuated with an inter-digitating comb drive (Fig. 1(b)). Their results show that the initial 2–4 nm thick SiO_2 layer thickens to approximately ~30–100 nm after cyclic deformation at a voltage of 40–100 V for cycles. They also show clear evidence of stress corrosion cracks (such cracks may be formed after releasing in HF, or stress-assisted crack nucleation and growth mechanisms) in the topical SiO_2layer after cyclic loading.[16] These results are shown schematically in Fig. 14(a).

In an effort to examine the regimes in which crack growth can occur, a linear elastic fracture mechanics framework is utilized to identify the conditions for stable and unstable crack growth in the SiO_2 layer. Figure 14(b) shows a schematic diagram of the crack in the SiO_2 layer on the Si. Beuth[27] and Ye et al.[28] analyzed the crack morphology using finite element analysis and presented a best-fitting expression for the energy release rate under a wedge load for a large number of material systems. The energy release rate, G, for the crack is given by

$$G = \frac{\sigma_0^2 h}{\bar{E}_f}\omega_f \tag{12}$$

where σ_0 is the wedge load on the crack, h is the thickness of the film, E_f is the Young's modulus of the film and ω_f is the

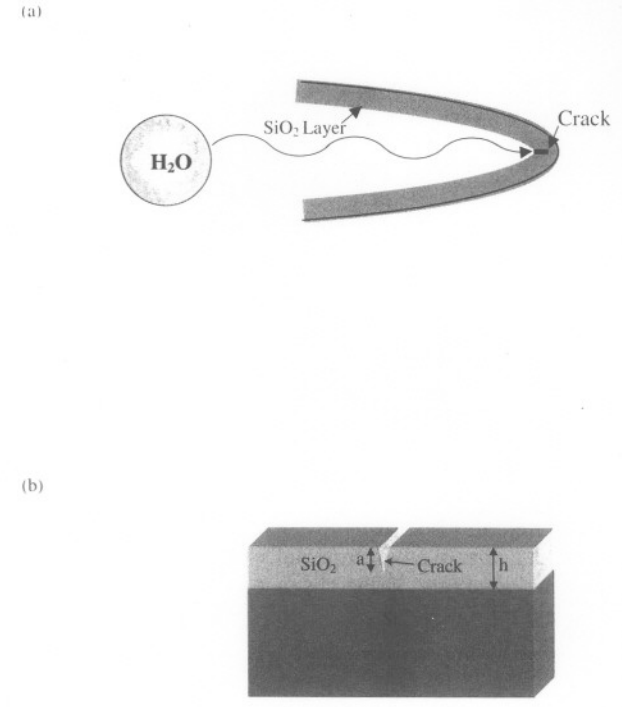

Fig. 14—Schematic representations: (a) stress corrosion cracking in SiO_2 layer; (b) schematic diagram of the crack in the topical SiO_2 layer over Si

non-dimensional number depending on the crack length, film thickness, and elastic properties of the film and the substrate. For this particular geometry, the non-dimensional number, ω_f, is determined by fitting to the full numerical solution and is expressed as

$$\omega_f = 3.951\frac{a_f}{h}\left(1-\frac{a_f}{h}\right)^{1-2s}\left(1+\lambda_1\frac{a_f}{h}\right)^2 \qquad (13)$$

where a_f is the crack length, s is the coefficient dependent on elastic properties of film and substrate, and λ_1 is a fitting parameter. For the present situation of SiO_2 film (E = 72 GPa and $\nu = 0.22$[28]) over Si substrate (E = 169 GPa and $\nu = 0.22$[18]), the coefficient, s, and the fitting parameter, λ_1, are approximately equal to 0.425 and –0.0437, respectively.[28]

The rms average of the notch-tip stress computed using finite element analysis for an actuation voltage of 145 V and material properties of SiO_2 and Si were used to compute energy release rates as a function of crack length for different thicknesses of the SiO_2 layer. The results of the energy release rate calculations are presented in Fig. 15(a). The fracture energy of SiO_2 ($\sim$ 6 Jm^{-2} [28]) and the threshold for stress corrosion cracking ($\sim$ 2 Jm^{-2} for a relative humidity of 70%[29]) are also compared with computed energy release rates in Fig. 15(a). The comparison indicates that stable crack growth due to strain corrosion cracking may occur in SiO_2 layers of thicknesses greater than $\sim$20 nm and transition to unstable crack growth may occur for layer thicknesses greater than $\sim$60 nm.

The calibration curve, eq (1), and results of finite element analysis, eq (2), were used to express the notch-tip stress and, subsequently, the energy release rate as a function of the actuation voltage

$$G = K\frac{V^4 h}{\bar{E}_f}\omega_f \qquad (14)$$

where K is the proportionality constant and is approximately $\sim 1.1 \times 10^{10}$ for the present MEMS structure. The resulting expression of the energy release rate, eq (14), was utilized to compute the values of actuation voltage corresponding to threshold for stress corrosion cracking and fracture for different crack lengths and thicknesses of SiO_2 layer. The computed actuation voltages for four different SiO_2 layer thicknesses (10, 20, 60, and 100 nm) are presented in Fig. 15(b).

The above results are consistent with the results of Muhlstein et al.[16] in which oxide thickening and stress corrosion cracking have been reported in polysilicon MEMS structures with an oxide thickness of $\sim$30–100 nm. Since the maximum energy release rate for SiO_2 film with thickness below $\sim$20 nm is less than the stress corrosion cracking threshold, stable subcritical crack growth in the polysilicon layer is unlikely until the topical oxide film thickness exceeds $\sim$20 nm. Similarly, the computed plots of energy release rate versus nominal crack length suggest that the onset of fracture instability is unlikely to occur until the oxide thickness exceeds $\sim$60 nm. This again is consistent with the results of Muhlstein et al.[16] in which maximum oxide thicknesses of $\sim$100 nm were observed using high voltage TEM.

Implications

The implications of the above results are quite significant. First, they suggest that surface topography can evolve due to stress-assisted dissolution in the topical SiO_2 layer. However, such stress-assisted dissolution is unlikely to control the nucleation unless the oxide thicknesses are below $\sim$20 nm. Instead, fatigue damage by stable stress corrosion cracking is likely to occur for oxide thicknesses greater than $\sim$20 nm. Since the crack driving force increases with increasing oxide thickness and crack length, unstable crack growth will initiate when the critical crack driving force for SiO_2 ($\sim$6 Jm^{-2}) is reached. Since this is comparable to Si fracture toughness, unstable crack growth in the SiO_2layer will result in unstable crack extension into the Si substrate.

Before closing, it is important to discuss the relative importance of surface topography evolution/oxidation versus crack growth mechanism. The above analyses shows that surface topography evolution may lead to crack nucleation only when the initial groove depths are much deeper than the cracks that are introduced during the HF release step. Furthermore, the driving force for the growth of the stress corrosion cracks along with the thickening of the topical SiO_2 layer. Although the mechanism for the oxide thickening is not fully understood, it is thought to be driven by the super saturation of polysilicon that occurs during chemical vapor deposition (CVD). Upon the application of cyclic stresses, the oxygen diffuses to the silicon/silica interface. This is most likely to happen during the tensile part of the loading cycle where atomic bonds are stretched. Upon arrival at the interface, oxygen atoms can react with Si to form SiO_2. This results ultimately in thickening of the topical SiO_2 layer from the bottom, as shown schematically in Fig. 16.

In many ways, the thickness of the SiO_2 layer sets the size scale for the crack driving force. When the SiO_2 layer

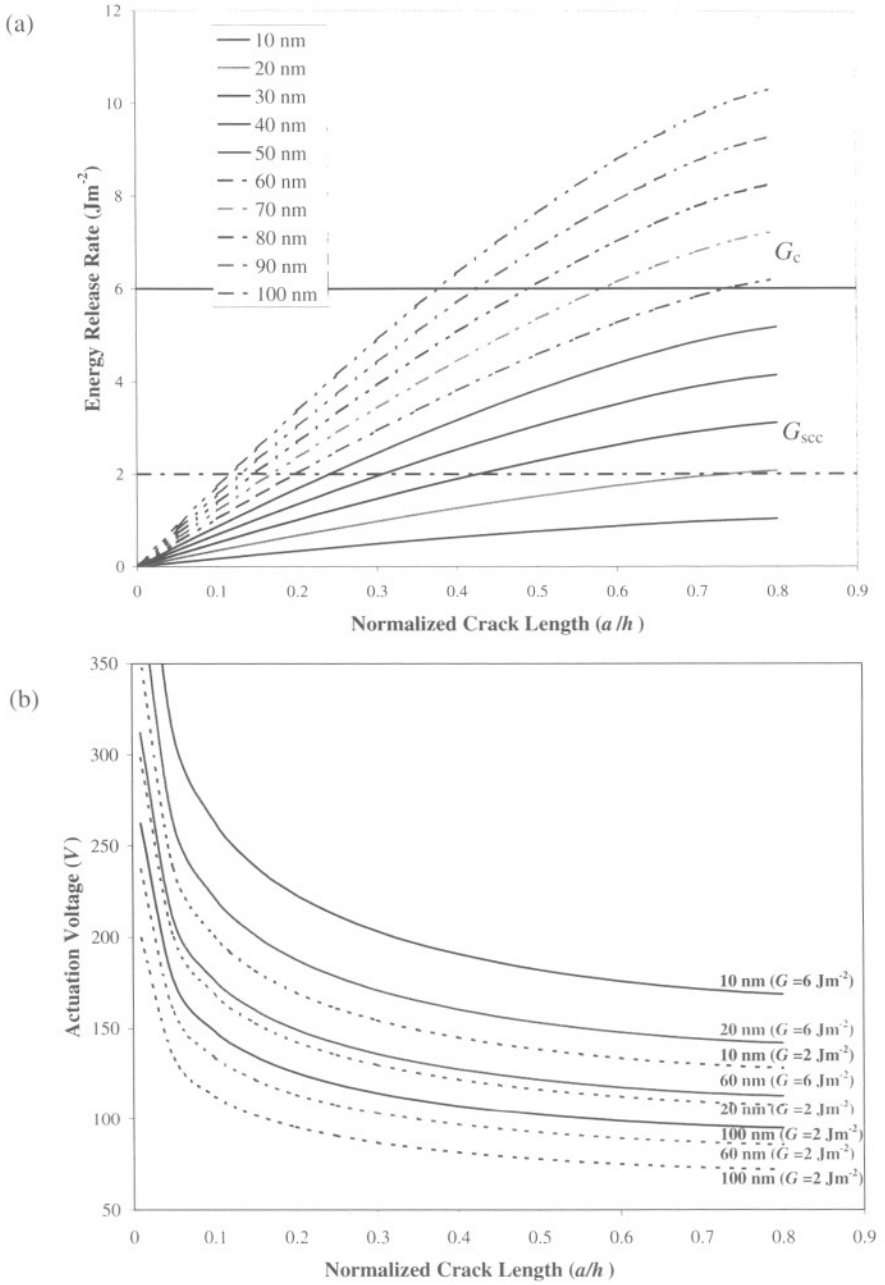

Fig. 15—Energy release rate calculations. (a) Computed energy release rates as a function of cracks length in the topical SiO_2 layer for different layer thicknesses, (b) Computed critical actuation voltages corresponding to threshold for stress corrosion cracking and fracture for different crack lengths and thicknesses of SiO_2 layer

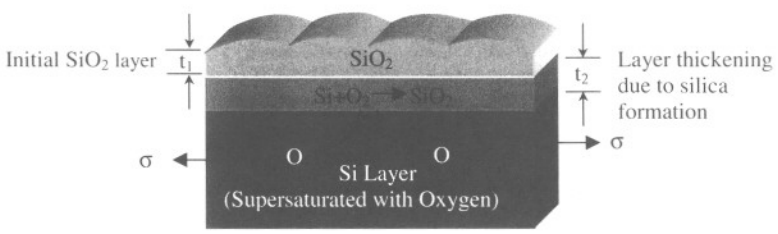

Fig. 16—Schematic diagram of oxide thickening mechanism

is greater than a certain thickness (~30 nm in Fig. 15(a)), the crack driving force exceeds the crack growth threshold for stress corrosion cracking, and hence stable crack growth can occur in the topical SiO_2 layer. Further thickening of the oxide layer (presumably by the same mechanism illustrated in Fig. 16) would lead ultimately to the SiO_2 fracture toughness being exceeded when the oxide layer thickness exceeds the critical thickness (~60 nm in Fig. 15(a)). Moreover, since the fracture toughness of the Si is comparable to that of the SiO_2 layer, unstable crack growth in the SiO_2 layer will result in unstable crack growth in the Si substrate. The thickening of the topical oxide layer, therefore, plays a crucial role in enhancing the driving force for crack growth in polysilicon MEMS structures.

Summary and Concluding Remarks

1. Surface topography evolution can occur during the cyclic actuation of Si MEMS structures. The surface evolution may be explained by stress-assisted dissolution in the topical SiO_2 layer that forms and thickens on the polysilicon substrate under cyclic actuation. The wavelengths that grow are consistent with predictions from a linear perturbation analysis.

2. Stable crack growth may occur from pre-existing cracks in the topical SiO_2 layer formed during specimen release or fabrication. Cracks may also nucleate due to the evolution of microgrooves into cracks. In any case, linear elastic fracture mechanics reveals that stable crack growth can occur in the SiO_2 layer when the energy release rate exceeds the stress corrosion cracking threshold. The possibility of stress corrosion cracking is also enhanced by the thickening of the SiO_2 layer that occurs during cyclic actuation.

3. Depending on the thickness of the topical SiO_2 layer, a transition from stable to unstable crack growth may occur when the energy release rate exceeds the fracture energy of SiO_2.

4. Stable crack growth is associated with stress corrosion cracking in the SiO_2topical layer when the oxide thicknesses are greater than a certain thickness (~30 nm in Fig. 15(b)). A transition from stable stress corrosion cracking to unstable crack growth (catastrophic failure) is expected when the oxide thickness reaches a critical value (~60 nm in Fig. 15(b)).

Acknowledgments

The research is supported by the Division of Mechanics and Materials of the National Science Foundation (Grant No CMS 0071483). Appreciation is extended to the program manager, Dr. John Larsen-Basse, for his encouragement and support. The authors are also grateful to Prof. Robert Ritchie and Prof. Chris Muhlstein for useful technical discussions.

References

1. Madou, M., Fundamentals of Microfabrication, 2nd edition, CRC Press, New York (2002).

2. Roming, A.D., "Opportunities and Challenges in MEMS Commercialization," Vacuum Technology and Coating (2001).

3. Brown, S.B., Van Arsdell, W., and Muhlstein, C.L., "Materials Reliability in MEMS Devices," International Solid State Sensors and Actuators Conference (Transducers '97), Chicago, IL (1997).

4. Jones, P.T., Johnson, G.C., and Howe, R.T., "Fracture Strength of Polycrystalline Silicon," presented at Microelectromechanical Structures for Materials Research-Symposium N (1998).

5. LaVan, D. and Buchheit, T.E., "Testing of Critical Features of Polysilicon MEMS," presented at Symposium MM, Materials Science of Microelectromechanical Systems (MEMS) Devices II, Boston, MA (1999).

6. Brown, S.B., Arsdell, W.V., and Muhlstein, C.L., "Materials Reliability in MEMS Devices," Transducers 97, International Conference on Solid-State Sensors and Actuators, Digest of Technical Papers (1997).

7. Kahn, H., Ballarini, R.L., Mullen, R., and Heuer, A.H., "Electrostatically Actuated Failure of Microfabricated Polysilicon Fracture Mechanics Specimens," Proc. Roy. Soc., Series A (Mathematical, Physical and Engineering Sciences), **455**, *3807–3823 (1999).*

8. Kapels, H., Aigner, R., and Bider, J., "Fracture Strength and Fatigue of Polysilicon Determined by A Novel Thermal Actuator [MEMS]," 29th European Solid-State Device Research Conference, Leuven, Belgium (1999).

9. Muhlstein, C.L., Brown, S., and Ritchie, R.O., "High Cycle Fatigue of Polycrystalline Silicon Thin Films in Laboratory Air," Materials Science of Microelectromechanical System (MEMS) Devices III, Boston, MA (2000).

10. Muhlstein, C.L., Brown, S., and Ritchie, R.O., "High Cycle Fatigue of Single Crystal Silicon Thin Film," J. Microelectromech. Syst., **10**, *593–600 (2001).*

11. Muhlstein, C.L., Howe, R.T., and Ritchie, R.O., "Fatigue of Polycrystalline Silicon for MEMS Applications: Crack Growth and Stability under Resonant Loading Conditions," Mechanics of Materials (2002).

12. Allameh, S.M., Gally, B., Brown, S., and Soboyejo, W.O., "On the Evolution of Surface Morphology of Polysilicon MEMS Structures During Fatigue," Materials Science of Microelectromechanical System (MEMS) Devices III, Boston, MA (2000).

13. Ritchie, R.O., "Mechanisms of Fatigue Crack Propagation in Ductile and Brittle Solids," Int. J. Fract., **100**, *55–83 (1999).*

14. Suresh, S., Fatigue of Materials, 2nd edition, Cambridge University Press (1998).

15. Kahn, H., Tayebi, N., Ballarini, R.L., Mullen, R., and Heuer, A.H., "Fracture Toughness of Polysilicon MEMS Devices," 10th International Conference on Solid State Sensors and Actuators (Transducers '99), Sendai, Japan (1999).

16. Muhlstein, C.L., Stach, E.A., and Ritchie, R.O., "Mechanism of Fatigue in Micron-scale Films of Polycrystalline Silicon for MEMS Applications," Appl. Phys. Lett. (2001).

17. Allameh, S.M., Gally, B., Brown, S., and Soboyejo, W.O., "Surface Topology and Fatigue in Si MEMS Structures," in Mechanical Properties of Structural Films, Vol. STP 1413, 3–16, C.L. Muhlstein and S. Brown, eds., American Society for Testing and Materials, West Conshohocken, PA (2001).

18. Sharpe, W.N., "Variation in Mechanical Properties of Polysilicon," 43rd International Symposium of Instrumentation Society of America, Orlando, FL (1997).

19. Kim, K.-S., Hurtado, J.A., and Tan, H., "Evolution of Surface-roughness Spectrum Caused by Stress in Nanometer-scale Chemical Etching," Physical Review Letters, **83**, *3872–3875 (1999).*

20. Bergen, J.R., Anandan, P., Hanna, K., and Hingorani, R., "Hierarchical Model-based Motion Estimation," Proceedings of Second European Conference on Computer Vision (1992).

21. Yang, W.H. and Srolovitz, D.J., "Surface Morphology Evolution in Stressed Solids: Surface Diffusion Controlled Crack Initiation," J. Mech. Phys. Solids, **42**, *1551–1574 (1994).*

22. Yu, H.H. and Suo, Z., "Delayed Fracture of Ceramics Caused by Stress-dependent Surface Reactions," Acta Meter., **47**, *77–88 (1999).*

23. Mullins, R., "Theory of Thermal Grooving," J. Appl. Phys., **28**, *333–339 (1957).*

24. Srolovitz, D.J., "On the Stability of Surfaces of Stressed Solids," Acta Metall. Mater., **37**, *621–625 (1989).*

25. Yu, H.H. and Suo, Z., "Stress-dependent Surface Reactions and Implications for a Stress Measurement Technique," J. Appl. Phys., **87**, *1211–1218 (2000).*

26. Iler, R.K., Chemistry of Silica, Wiley, New York (1979).

27. Beuth, J.L., "Cracking of Thin Bonded Films in Residual Tension," Int. J. Solids Struct., **29**, *1657–1675 (1992).*

28. Ye, T., Suo, Z., and Evans, A.G., "Thin Film Cracking and the Roles of Substrate and Interface," Int. J. Solids Struct., **29**, *2639–2648 (1992).*

29. Lawn, B.R., Fracture of Brittle Solids, 2nd edition, Cambridge University Press, Cambridge (1993).